High power ytterbium rod-type fiber laser delivering tunable picosecond pulses.

Muhammad Ghawas, Valerian Freysz, Lukas Muller, Sébastien Cassagnère, Eric Freysz

High power ytterbium rod-type fiber laser delivering tunable picosecond pulses

MUHAMMAD GHAWAS,[1] VALERIAN FREYSZ,[1] LUKAS MÜLLER, [1] SÉBASTIEN CASSAGNÈRE,[1] AND ERIC FREYSZ[1,*]

[1] *Univ. Bordeaux, CNRS, LOMA, UMR 5798, F-33400 Talence, France*
[*] *eric.freysz@u-bordeaux.fr*

Abstract: We designed an all-normal dispersion ytterbium rod-type fiber laser oscillator delivering picosecond pulses which are continuously tunable both in central wavelength and pulse duration. This system delivers self-mode-locked pulses with an average power up to 25 W. At a repetition rate of 78 MHz, it yields picosecond laser pulses, of which the central wavelength and pulse duration can be tuned between 1010 nm - 1060 nm and 4.5 ps - 1.8 ps, respectively. The tunability is obtained by adjusting the position and the width of a slit which acts as a spectral bandwidth filter, placed close to the center of a 4f-folded zero dispersion line inserted in the laser cavity. This oscillator delivers nearly Fourier limited pulses with at most a 1.2 time-bandwidth product. A numerical model accounts well for the behavior of this all-normal dispersion fiber oscillator.

1. Introduction

High power picosecond lasers have been used in many different fields, for instance, precision manufacturing [1], to study ultrafast dynamics [2], photovoltaic and semiconductor devices [3,4], etc. Fiber laser sources have been shown to be very useful in nonlinear microscopy [5,6], diffuse optical spectroscopy [7], and nonlinear frequency conversion [8]. Fiber lasers delivering picosecond pulses have a broad range of industrial and research applications, for example, material processing [9], biomedical research [10], supercontinuum generation [11], frequency doubling [12], and source to pump optical parametric oscillators [13]. Hence, during the last few decades, the use of fibers to generate picosecond pulses has grown remarkably in all aspects, due to their excellent attributes, such as, thermal management, compactness, robustness, easy alignment, and better beam quality [14,15]. Erbium doped fiber laser providing tunable picosecond pulses in the Telecom wavelength in the 1.532 µm to 1.594 µm range have been reported [16]. Ytterbium (Yb) doped fiber is among the most popular fibers due to its broad-gain-bandwidth and small quantum defect [17,18], and it has been previously used to generate picosecond pulses around 1 µm [19–30]. All-normal-dispersion (ANDi) fiber along with a birefringent filter was used to generate tunable picosecond pulses, but the output average power was limited to ~ 60 mW [28]. Diffraction grating instead of birefringent filter was also used as a spectral filter, the tunability being achieved by changing the angle of incidence (AOI) on the grating which, we think, may degrade the efficiency in terms of output average power [30]. In combination with gratings, a semiconductor saturable absorber mirror (SESAM) was implemented to generate tunable self-starting pulses [19,27]. But this makes the laser cavity complicated and also limits the output average power to below ~ 30 mW. Wavelength tunable self-starting fiber laser in which mode-locking was ensured with the bulk phase modulator has also been reported but here again the average power was limited to 38 mW [25]. It has also been shown that a programmable digital micro-mirror device can be used in combination with a grating in the ytterbium-doped fiber cavity to ensure central wavelength tunability from 1020 nm to 1060 nm [29].

In this paper, we demonstrate high power laser source delivering picosecond pulses with tunability both in central wavelength and spectral width. This ring laser is built around a large-

mode-area (LMA) dual clad ytterbium fiber. The central laser wavelength and duration of the generated pulses are adjusted by implementing a 4f-folded zero dispersion line in the laser cavity. A slit that acts as a spectral bandwidth filter is inserted near the focal plane of the lens. Changing the position and width of this slit makes it possible to tune the central wavelength and duration of the generated pulses, respectively. The self-starting pulsed laser operation is achieved in the laser cavity by optimizing the nonlinear polarization rotation (NPR) [31] in the LMA ytterbium fiber which in-result generates high power almost Fourier-limited picosecond pulses. The central wavelength of these pulses is continuously adjusted over 50 nm from 1010 nm to 1060 nm, while the spectral width is tuned from 0.38 nm up to 2.24 nm. At its fundamental repetition rate of 78 MHz, the maximum extracted average power is around 25 W, which corresponds to a pulse energy of about 320 nJ. We also demonstrate that numerical model previously reported well accounts for our experimental results [32].

2. Experimental setup

The ring laser configuration shown in Fig. 1a is arranged around a LMA rod-type ytterbium-doped fiber (NKT photonics, AeroGAIN-ROD modules, Model 1.1). The length of the fiber is 0.8 m, and it has a mode field diameter of 45 ± 4 µm and a pump-cladding diameter of 200 ± 10 µm at 1030 nm. The fiber is pumped by a 2 nm broad laser diode at 976 nm through a dichroic mirror which has a high reflectivity at 1030 nm and high transmissivity around 976 nm. Mode-locking of the fiber laser is achieved by taking advantage of the nonlinear polarization rotation (NPR) inside the LMA ytterbium fiber. Thanks to the NPR along with the combination of two $\lambda/4$-waveplates (QW1, QW2), one $\lambda/2$-waveplate (HW1), optical isolator (OI), called hereinafter nonlinear output port (NLOP), only the high-intensity part of the pulses is transmitted inside the laser cavity, imitating the principle of operation of saturable absorber (SA). A transmission grating (TG) having a period of 575 nm (1739 lines/mm) is inserted inside the laser cavity to disperse the pulse beam (AOI = 63.6°, s-polarized) into its spectral components. With a lens having a focal length of 75 mm, the dispersed light is collimated and imaged onto a high reflecting mirror (HRM). The reflected light from the HRM is sent back through the transmission grating and propagates through the ring laser cavity. The transmission grating and the mirror are kept at twice the focal length of the lens in a 4f-folded dispersion line. With this 4f-folded system, the dispersion of the grating can be almost cancelled and if necessary can be finely adjusted within the laser cavity. A mechanical slit (VA100-Thorlabs) is placed on a translation stage in front of the HRM. When the slit is set near the focal plane of the lens, it makes it possible to adjust the spectral width and central wavelength of the generated pulses. Hence, the slit size is varied to tune the spectral width of the spectrum whereas its position adjusts the central wavelength of the generated pulses. The isolator after the $\lambda/2$-plate (HW1) ensures the unidirectional flow inside the laser cavity, and the laser output is achieved through a polarizing beam splitter (PBS) attached at the end of the isolator. The output pulses are detected with a 2 GHz Si-based photo-detector (Thorlabs DET025/M) and analyzed using an oscilloscope (RIGOL MSO5204) while their spectra are measured using an optical spectrum analyzer (Thorlabs OSA205C). Similarly, the RF spectrum of the pulses is analyzed using an RF spectrum analyzer (Agilent Technologies N9340B). Lastly, the pulse duration is measured by a homemade intensity autocorrelator using a BBO crystal (type I phase matching at 1030 nm).

3. Experimental results and discussion

In this section, the results obtained from our laser setup are discussed. The pump threshold power of our fiber laser is ~ 17 W. Above this pump power, we improved the output power by rotating the waveplates. The slope efficiency of around 47 % was achieved for the CW output. Mode-locking is achieved with about 65 W of pump power. To ensure stable mode-locking regime, the waveplates are optimized. Their optimized angles are QW1 = 141°, QW2 = 129°,

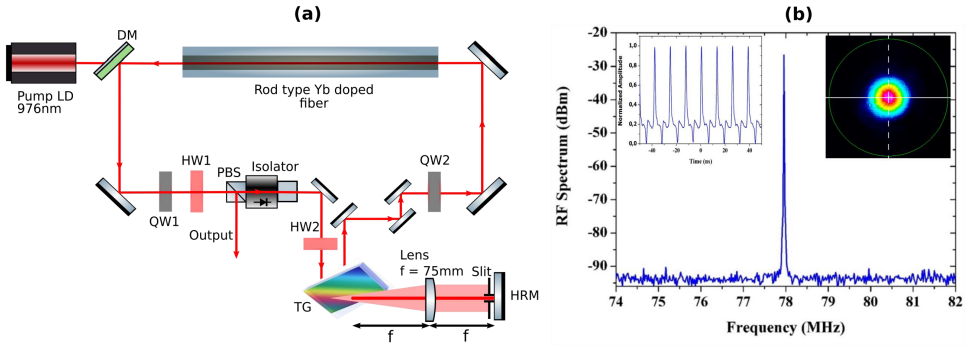

Fig. 1. (a) Ytterbium-doped rod-type fiber laser setup. LD: laser diode, DM: Dichroic mirror, HW: Half waveplate, QW: Quarter waveplate, TG: transmission grating, PBS: polarizing beam splitter, and HRM: high reflection mirror. (b) The RF spectrum ($\sim$ 65 dBm) at a resolution bandwidth (RBW) of 1kHz, shows the fundamental repetition rate around 78 MHz, (Inset left: Oscilloscope trace of the laser pulses, Inset right: Pulse beam profile)

and HW1 = 99°, respectively. The RF spectrum recorded with a resolution bandwidth of 1 kHz and oscilloscope trace of the output pulse centered at 1030 nm are plotted in Fig. 1b. The fundamental repetition rate is close to 78 MHz and the signal-to-noise peak is about $\sim$ 65 dB indicating a stable pulse mode-locking. The pulse beam profile ($M^2 \leq 1.3$) is plotted in the inset (right) in Fig. 1b. In order to continuously adjust the spectral width and the central wavelength of the generated pulses, we made sure that the laser is robustly self mode-locking. This is accomplished by precisely adjusting the distance from the TG to the lens, and from the lens to the HRM. Hence, both the lens and the HRM are mounted on precision translation stages to keep the distances between the TG to the lens and from the lens to the HRM almost equal to the focal length of the lens. Even if the slit is placed almost against the HRM, still it is not exactly in the focal plane of the lens. This implies that the slit is not sharply filtering the spectrum of the laser pulse. This is why, in the simulations presented afterwards in the manuscript, we will consider the slit acts as a super-Gaussian filter of low order.

3.1. Spectral width tunability

The spectral width of the output pulses is continuously adjusted by changing the size of the slit. Figure 2a displays the evolution of the pulse spectrum for a pump power of 78 W. Around a 1030 nm central wavelength, as the width of the slit increases from 0.26 mm to 0.70 mm, the spectral width (full-width at half maximum (FWHM): $\Delta\lambda$) of the pulse spectra broadens from $\sim$ 0.38 nm to $\sim$ 2.24 nm. Even if the pulse spectral profiles are structured, the FWHM spectral width and the root mean square spectral width deviates from each other by less than 3%. The broadening of the pulse spectra is concomitant with the reduction of the duration of the autocorrelation at half-width (τ_{ac}). The latter decreases from $\tau_{ac} = 6.3 \pm 0.1$ ps (corresponds to the spectral width of $\sim$ 0.38 nm) down to $\tau_{ac} = 2.5 \pm 0.1$ ps (corresponds to the spectral width of $\sim$ 2.24 nm) (Fig. 2b). Considering a Gaussian pulse, this indicates the pulse duration τ_p decreases from $\sim$ 4.5 ps to $\sim$ 1.8 ps. The reduction of the pulse duration is accompanied by a decrease of the average output power from $P_{out} \sim 24.3$ W to $P_{out} \sim 17.6$ W (Fig. 2c). Accordingly, the pulse energy reduces from $E_p \sim 312$ nJ to $E_p \sim 225$ nJ. However, while the pulse energy decreases, the pulse peak power increases from $P_p \sim 70$ kW to $P_p \sim 129$ kW. This ultimately modifies the self-phase modulation (SPM) experienced by the laser pulse during its propagation in the ytterbium fiber and broadens its output pulse spectrum. The evolution of

the spectral width of the generated pulses versus the width of slit is displayed in Fig. 2d. As noted in the figure, the spectral width of the pulses varies nonlinearly with respect to the slit size. The reduction of the average power recorded while enlarging the slit width is likely due

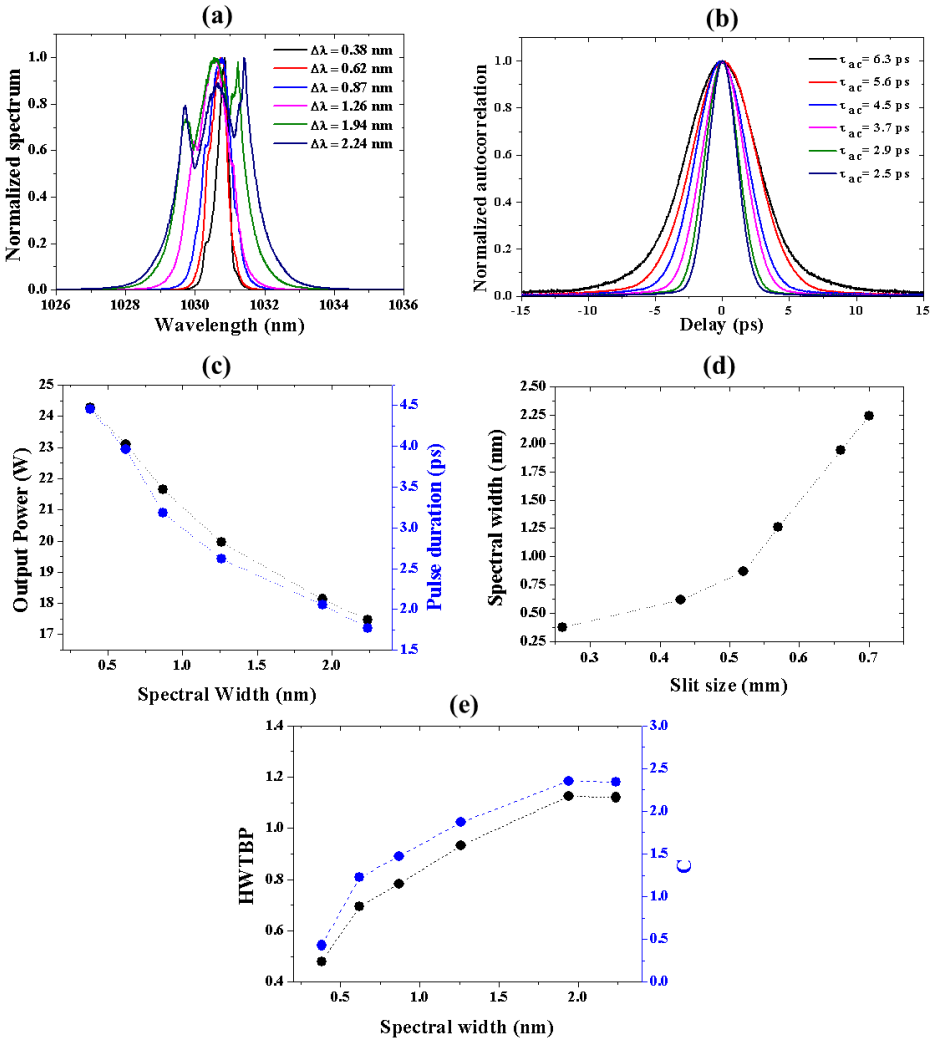

Fig. 2. (a) Output pulse spectra recorded while changing the slit width. (b) Corresponding intensity autocorrelation traces. (c) Evolution of the average output power and pulse duration versus the spectral width of the generated pulse. (d) Variation of the spectral width of the pulses according to the slit size. (e) Evolution of the half-width time-bandwidth product (HWTBP) and the chirp parameter C versus the pulse spectral width. The lines in figures c,d and e are guide for the eyes.

to SPM. As the SPM increases, the pulse spectrum broadens and it experience more losses during its transmission through the slit. Similarly, the increase of SPM results in an increase of the half-width time bandwidth product (HWTBP). Considering the envelope of the pulse is Gaussian in shape, the parameter C of the chirped pulse is computed as $\tau_p = \tau_p^0\sqrt{1+C^2}$, where τ_p and τ_p^0 are the pulse duration of the chirped and unchirped pulses, respectively. The latter is computed using the Fourier transform of the pulse spectra. The chirp parameter C increases

from ~ 0.4 to ~ 2.35 as the width of the slit is enlarged (Fig. 2e). Based on the data in Fig. 2a and Fig. 2b, we computed the HWTBP which is plotted in Fig. 2e. It increases from 0.47 (almost Fourier-limited if Gaussian pulse is considered) to 1.14 as the size of the slit is enlarged. Additionally, sharp peaks are observed at the edges of the spectrum when the spectrum gets broader ($\Delta\lambda$ = 1.26 nm, 1.94 nm and 2.24 nm) as a result of the increase of SPM (Fig. 2a) [32].

3.2. Central wavelength tunability

As mentioned in the setup description, the central wavelength of the generated pulses can also be changed, while ensuring the fiber laser is self mode-locked, keeping the width of the slit constant and varying its position laterally. Figure 3a shows the recorded spectra varying the position of the slit for a pump power of 81 W, demonstrating a 50 nm tunability over the 1010 nm to 1060 nm spectral range. The minimum spectral width of 0.62 nm is recorded at 1024 nm and the maximum spectral width of 0.88 nm is recorded at 1059 nm, respectively. The autocorrelation

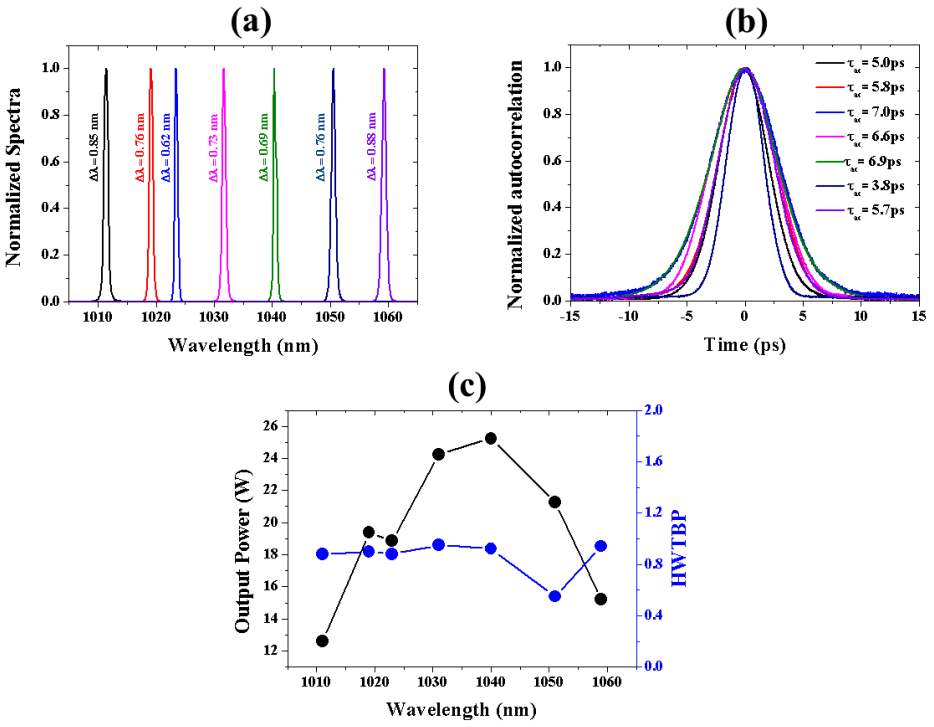

Fig. 3. (a) Tunability of the central wavelength achieved while keeping the constant slit width. (b) Corresponding autocorrelation traces. (c) Average output power and half-width time-bandwidth product (HWTBP) versus the wavelength. The lines in (c) are guide for the eyes.

traces of the generated pulses are displayed in Fig. 3b. The maximum and minimum durations of the autocorrelation at half-width τ_{ac}^{max} = 7.0 ± 0.1 ps and τ_{ac}^{min} = 3.8 ± 0.1 ps are recorded at 1024 nm and 1051 nm, respectively. Considering Gaussian pulses, the pulse duration is written as, $\tau_p^{min,max} = \tau_{ac}^{min,max}/\sqrt{2}$. According to the data displayed in Fig. 3a and Fig. 3b, the half-width time-bandwidth product (HWTBP) is plotted in Fig. 3c. The average output power for these spectra is also shown in the same figure. The evolution of average output power is bell shaped and it is in good agreement with the emission cross-section of ytterbium-doped optical fiber [17]. A maximum of ~ 25 W of average power is achieved ~ 1040 nm. Towards the edges

(i.e., at 1010 nm and 1060 nm) the output average power is decreased to ~ 13 W, and ~ 15 W, respectively. Based on the average power and the pulse duration, the minimum and maximum peak power, achieved at 1010 nm and 1051 nm, are ~ 46 kW and ~ 101 kW, respectively. The HWTBP is almost constant and around 0.90 for all spectra except for the spectrum at 1051 nm where the HWTBP is 0.55.

4. Numerical model and discussion

To account for the above reported behaviors of our fiber laser, we run a numerical model previously reported in [32]. The computations were performed considering the laser is built around a 0.8 m long, single mode ytterbium-doped fiber having mode field diameter $d_0 = 50\,\mu$m. The pulse is then freely propagated in the air for a length of 2.67 m before being sent through a saturable absorber (SA) that mimics the role of the NPR in combination with the NLOP [32]. The output mirror of the laser is set just after the SA with a 70% coupling ratio. Before being amplified again in the fiber, the pulse is transmitted through a super-Gaussian filter of order $n = 3$. This filter accounts for the role of the slit slightly displaced from the focal plane of the 4f-folded dispersion line. As we already mentioned, in the presentation of the set-up, this implies the slit is not sharply filtering the spectrum of the pulses. Results for Gaussian and super-Gaussian filters of order $n = 2, 3, 5, 10$ with a given width of 0.3 nm centered at 1030 nm, are presented in the supplementary materials. Previous study has shown that the Gaussian spectral filter impacts the pulse breaking-up process whereas super-Gaussian-shaped filter give rise to noise-like pulses in all-normal-dispersion fiber lasers [33]. Thanks to the moderate pump power we used, no such effects are evidenced in our simulations. During the propagation in the fiber, the laser pulse experiences amplification and self-phase modulation. The propagation of the laser pulse within the amplifying fiber is simulated by solving the nonlinear Schrödinger equation:

$$\frac{\partial A}{\partial z} + i\frac{\beta_2}{2}\frac{\partial^2 A}{\partial \tau^2} = \frac{g}{2}A + i\gamma(\omega_0)|A|^2 A, \tag{1}$$

where $A = A(z, \tau)$ is the slowly varying envelope of the pulse, z is the propagation coordinate, τ is the time delay parameter, and β_2 is the group velocity dispersion. γ is the nonlinear parameter given by $\gamma(\omega_0) = 4n_2\omega_0/(c\pi d_0^2)$ where n_2 is the Kerr coefficient, ω_0 is the central angular frequency, c is the velocity of light in vacuum. The gain g within the fiber is written as $g = g_0/(1 + E_{pulse}/E_{sat})$, where g_0 is the small signal gain, E_{sat} is the gain saturation energy, $E_{pulse} = \int_{-T_R/2}^{+T_R/2} |A|^2 d\tau$ and T_R is the cavity round trip time. The transmission function of the SA is given as, $T = 1 - q_0/[1 + P(\tau)/P_{sat}]$ where q_0 is the unsaturated losses, $P(\tau)$ is the instantaneous pulse power and P_{sat} is the saturation power. The numerical model is solved with a standard split-step algorithm and the initial field is white noise. We run our simulations considering $\beta_2 = 230\,\text{fs}^2/\text{cm}$, $n_2 = 2.19 \times 10^{-20}\,\text{m}^2/\text{W}$, $g_0 = 3.45\,\text{m}^{-1}$, $E_{sat} = 110\,\text{nJ}$, $q_0 = 0.55$ and $P_{sat} = 7\,\text{kW}$.

4.1. Spectral width tunability

To run these simulations, we adjusted the filter bandwidth (FBW) of the super-Gaussian filter from 0.23 nm to 1.2 nm. The simulated arrangement matched the experimental setup except for the SA. Indeed, in the experiment, the NLOP takes the role of the SA. But the NLOP has a sinusoidal transfer function whereas the SA has a monotonically increasing transfer function. Therefore, in the experiment, the output coupling depends on the NLOP parameters while it is assumed to be constant in the simulations. Despite these differences, numerical simulations shown in Fig. 4 are able to retrieve the experimental trends displayed in Fig. 2. At constant gain saturation energy E_{sat}, as we increase the spectral BW of the super-Gaussian filter, the output power P_{out} and pulse duration τ_p decrease from 28.2 W to 13.3 W and from 12.9 ps to 2.2 ps,

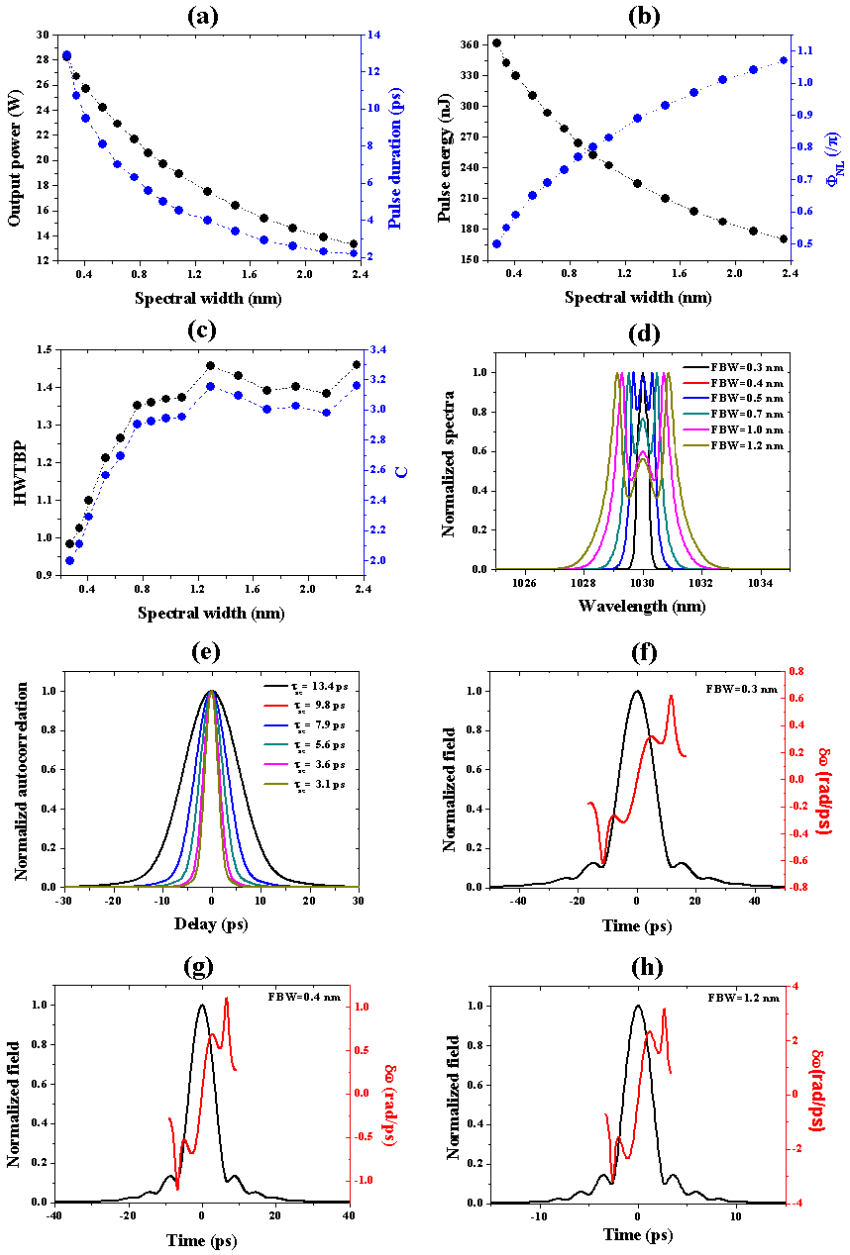

Fig. 4. Numerical simulations of the laser evolution. (a) Average output power and pulse duration versus the spectral width of the super-Gaussian filter. (b) Corresponding pulse energy and nonlinear phase shift Φ_{NL}. (c) Evolution of the half-width time bandwidth product and the chirp parameter C of the output pulses versus the spectral width of the filter. (d) Spectra of the output pulse for FBW of 0.3 nm, 0.4 nm, 0.5 nm, 0.7 nm, 1.0 nm and 1.2 nm, respectively. (e) Corresponding autocorrelation trace of the output pulses. (f–h) Normalized field envelope and frequency chirp ($\delta\omega$) for FBW of 0.3 nm, 0.4 nm, and 1.2 nm, respectively. The lines in figures a, b and c are guide for the eyes.

respectively (Fig. 4a). It is worth noticing that as the width of the spectral filter increases, while the energy of the pulse decreases from ~ 362 nJ to ~ 170 nJ, the pulse peak power increases from ~ 28 kW to ~ 77 kW. Accordingly, the nonlinear phase shift, experienced by the pulse during its propagation in the amplifying fiber, increases from 0.50π to 1.07π (Fig. 4b). We have also evaluated the HWTBP and chirp parameter C plotted in (Fig. 4c) which increases from ~ 0.98 to ~ 1.45 and from ~ 2.0 to ~ 3.2, respectively as the width of the slit is enlarged. As self-phase modulation increases, the edges of the pulse spectra grow substantially with a pronounced dip in the center (Fig. 4d). In good agreement with the experimental data (Fig. 2a), the half-width bandwidth of the pulse spectrum also increases from 0.27 nm to 2.35 nm (Fig. 4d). In Fig. 4f, 4g, and 4h we have also plotted the normalized field envelope and the frequency chirp ($\delta\omega$). The latter is related to the chirp parameter C [34]. The envelope of the pulse exhibits oscillations that last for about twice the pulse duration. The frequency chirp evolves almost linearly across the central part of the pulse but exhibits high-frequency oscillations outside. As the spectral width of the super-Gaussian filter increases, the pulse duration at half-width decreases whereas $\delta\omega$ increases.

As presented in the supplementary material the oscillations in the pulse envelope and $\delta\omega$ disappear if a Gaussian filter is used. The oscillations in pulse envelope and $\delta\omega$ are lasting longer and are more pronounced as the order of the super-Gaussian is increased. The latter behavior is expected due to the sharp edges of the super-Gaussian filter. Besides, the pulse energy and $\delta\omega$ are higher for super-Gaussian filter with higher order. This is expected since the transmission of the super-Gaussian filter of higher order is higher.

4.2. Central wavelength tunability

We have also simulated the evolution of the generated pulses for a given pump power considering a super-Gaussian filter of order n=3 having a width of 0.5 nm, while tuning its central frequency. To account for the evolution of the gain within the fiber versus the central wavelength of the super-Gaussian filter, the amplitude of the small signal gain g_0 was adjusted according to the evolution of the emission cross section of ytterbium [17]. The unsaturated gain $g_0(\lambda)$ at a given wavelength was computed considering $g_0(\lambda) = 3.45 \cdot \sigma(\lambda)/\sigma(\lambda = 1030\,\text{nm})$ where $\sigma(\lambda)$ is the emission cross section of ytterbium at the wavelength λ. To account for the increase of the pump power from 78 W to 81 W used to record the experimental data displayed in Fig.3, we increased E_{sat} from 110 nJ to 120 nJ in the simulations. The other numerical parameters are the same. Here again, the numerical simulations are able to retrieve the experimental trends displayed in Fig. 3. The maximum averaged output power P_{out} ~ 22.5 W is achieved around 1030 nm. Towards the edges of the scanned spectral range (i.e., at 1010 nm and 1055 nm) the output average power is decreased to 16.4 W and 15.3 W, respectively. The autocorrelation duration τ_{ac} of the generated pulses slightly changes (Fig. 5b). It increases versus the wavelength. It is about 7.6 ps and 8.8 ps at 1010 nm and 1060 nm, respectively. This corresponds to a Gaussian pulse duration τ_p of 5.4 ps and 6.2 ps, respectively. The pulse peak power P_p evolves smoothly and follows the same trend as the output power. It is ~ 39 kW at 1010 nm, increases to ~ 51 kW at 1030 nm, and then decreases to ~ 32 kW at 1060 nm. The nonlinear phase shift Φ_{NL} experienced by the laser pulse during its propagation in the fiber evolves accordingly. It is $\Phi_{NL} \approx 0.66\pi, 0.83\pi, 0.54\pi$ at λ = 1010 nm, 1030 nm and 1060 nm, respectively. As Φ_{NL} increases, the spectra of the generated pulses exhibit more sharper peaks at it edges. The value of HWTBP slightly evolves and follows the same trend as Φ_{NL}. It is ~ 1.22, 1.42, 1.07 at λ = 1010 nm, 1030 nm and 1060 nm, respectively. The normalized field envelope and $\delta\omega$ for three different central wavelengths (λ = 1010 nm, 1030 nm and 1060 nm) are also plotted in Figs. 5d, 5e, and 5f, respectively. For all the wavelengths, the envelope and the frequency chirp of the pulse are almost similar in shape. The frequency chirp slightly increases around 1030 nm where the nonlinear phase shift is higher.

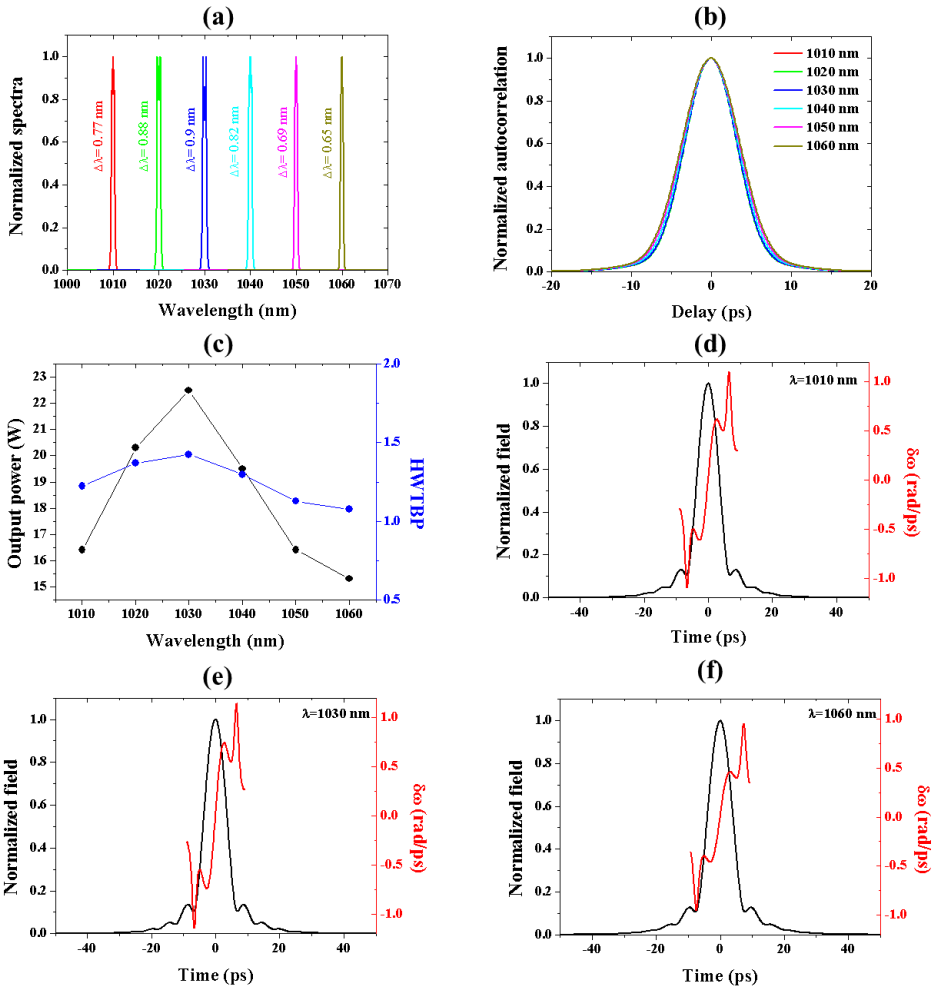

Fig. 5. Numerical simulation of the laser output evolution versus the wavelength. (a) Evolution of the spectra from 1010 nm to 1060 nm of the generated pulses considering a super-Gaussian filter of order $n = 3$ with a FBW of 0.5 nm. (b) Corresponding normalized autocorrelation traces. (c) Output power and half-width time-bandwidth product (HWTBP) versus the wavelength. (d–f) Normalized field envelope and frequency chirp ($\delta\omega$) for central wavelength of 1010 nm, 1030 nm, and 1060 nm, respectively. The lines in (c) are guide for the eyes.

4.3. Discussion

Overall the numerical simulations are able to account for the experimental behavior we recorded. While the numerical and experimental spectra and energies of the pulses are in good agreement, the experimental HWTBP is shorter from the numerical ones. As we already mentioned, this phenomenon can be associated with the difference of the transfer function of SA and NLOP. However, we also suspect the 4f-folded dispersion line to partly compensates for the frequency chirp experienced by the laser pulse during its propagation within the laser cavity. However, based on our simulations the remaining nonlinear frequency chirp will be difficult to compensate by conventional grating compressor.

5. Conclusion

In conclusion, we have developed a high power laser source delivering picosecond pulses with tunability both in central wavelength and spectral width. It incorporates a combination of a large-mode-area dual clad ytterbium fiber, a slit, and a transmission grating inside the ring laser cavity configuration. At $\lambda \sim 1030$ nm and with a repetition of 78 MHz, this laser delivers picosecond pulses with pulse duration τ_p which can be continuously adjusted from ~ 1.8 ps to ~ 4.5 ps and accordingly pulse energy from ~ 320 nJ and ~ 225 nJ, respectively. The pulses with the larger pulse duration are almost Fourier-limited (HWTBP~ 0.48) whereas for the shorter ones the HWTBP is at most about 1.2. We have also demonstrated the central wavelength of the laser pulse can be continuously tuned from $\lambda \sim 1010$ nm to $\lambda \sim 1060$ nm while keeping the pulse energy above ~ 150 nJ. Contrary to conventional femtosecond ANDi laser, to control the spectral width of the generated pulse while achieving an almost Fourier-limited picosecond pulse, our ANDi laser is running without adding any passive optical fiber in the laser cavity [32]. We have also adapted a previously proposed numerical model to account for the ensemble of our experimental data [32]. Our numerical simulations well capture the experimental trends. The different phenomena that can be responsible for the difference between the numerical and experimental data are proposed. This laser system offers many interesting features, to name a few, it can be used to pump picosecond optical parametric oscillators, supercontinuum generation, and biomedical imaging [35, 36].

Funding. This project was funded by the European Union's Horizon 2020 research and innovation program under the Marie Skłodowska-Curie grant agreement No. 813159, and the French National Research Agency (ANR) in the frame of "the investments for the future" Programme IdEx Bordeaux – LAPHIA (ANR-10-IDEX-03-02) and the Conseil Région Nouvelle-Aquitaine

Disclosures. The authors declare no conflicts of interest.

Data availability. Data underlying the results presented in this paper are not publicly available at this time but may be obtained from the authors upon reasonable request.

Supplementary materials. See Supplement 1 for supporting content.

References

1. R. Knappe, "Applications of picosecond lasers and pulse-bursts in precision manufacturing," in *Laser Applications in Microelectronic and Optoelectronic Manufacturing (LAMOM) XVII,* vol. 8243 (International Society for Optics and Photonics, 2012), p. 82430I.
2. S.-B. Zhu, J. Lee, and G. Robinson, "Effects of an intense picosecond laser on liquid carbon disulfide: a molecular dynamics study," JOSA B **6**, 250–256 (1989).
3. R. Moser, M. Kunzer, C. Goßler, K. Köhler, W. Pletschen, U. T. Schwarz, and J. H. Wagner, "Laser processing of gallium nitride-based light-emitting diodes with ultraviolet picosecond laser pulses," Opt. Eng. **51**, 114301 (2012).
4. J. A. Albelo, P. Y. Pirogovsky, J. N. O'Brien, and B. W. Baird, "Picosecond laser micromachining of advanced semiconductor logic devices," in *Solid State Lasers XVII: Technology and Devices,* vol. 6871 (International Society for Optics and Photonics, 2008), p. 687122.
5. Y. Liu, H. Tu, W. A. Benalcazar, E. J. Chaney, and S. A. Boppart, "Multimodal nonlinear microscopy by shaping a fiber supercontinuum from 900 to 1160 nm," IEEE J. Sel. Top. Quantum Electron. **18**, 1209–1214 (2011).
6. W. Liu, S.-H. Chia, H.-Y. Chung, R. Greinert, F. X. Kärtner, and G. Chang, "Energetic ultrafast fiber laser sources tunable in 1030–1215 nm for deep tissue multi-photon microscopy," Opt. express **25**, 6822–6831 (2017).
7. P. Taroni, A. Bassi, D. Comelli, A. Farina, R. Cubeddu, and A. Pifferi, "Diffuse optical spectroscopy of breast tissue extended to 1100 nm," J. biomedical optics **14**, 054030 (2009).
8. M. Klein, P. Gross, K.-J. Boller, M. Auerbach, P. Wessels, and C. Fallnich, "Rapidly tunable continuous-wave optical parametric oscillator pumped by a fiber laser," Opt. letters **28**, 920–922 (2003).
9. S. Nolte, C. Momma, H. Jacobs, A. Tünnermann, B. N. Chichkov, B. Wellegehausen, and H. Welling, "Ablation of metals by ultrashort laser pulses," JOSA B **14**, 2716–2722 (1997).
10. A. Bulter, R. Erdmann, and T. Schmitt, "Amplified picosecond diode lasers simplify biomedical research," Biophotonics Int. **12**, 38–41 (2005).
11. H. Chen, S. Chen, J. Wang, Z. Chen, and J. Hou, "35 W high power all fiber supercontinuum generation in PCF with picosecond MOPA laser," Opt. communications **284**, 5484–5487 (2011).

12. S.-u. Alam, K. Chen, J. R. Hayes, D. Lin, A. Malinowski, H. J. Baker, N. Trela, R. McBride, and D. J. Richardson, "Over 55W of frequency doubled light at 530 nm pumped by an all-fiber diffraction limited picosecond fibre MOPA," in *Fiber Lasers VII: Technology, Systems, and Applications,* vol. 7580 (International Society for Optics and Photonics, 2010), p. 758007.
13. P. Dupriez, A. Piper, A. Malinowski, J. Sahu, M. Ibsen, Y. Jeong, L. Hickey, M. Zervas, J. Nilsson, and D. Richardson, "321 W average power, 1 GHz, 20 ps, 1060 nm pulsed fiber MOPA source," in *Optical Fiber Communication Conference,* (Optical Society of America, 2005), p. PDP3.
14. J. Gabzdyl, "Fibre lasers make their mark," Nat. Photonics **2**, 21–23 (2008).
15. C. Jauregui, J. Limpert, and A. Tünnermann, "High-power fibre lasers," Nat. photonics **7**, 861–867 (2013).
16. G. Gao, Z. Zhao, Z. Cong, Q. Zhao, and Z. Liu, "Widely wavelength-tunable mode locked er-doped fiber oscillator from 1532 nm to 1594 nm with high signal-to-noise ratio," Opt. & Laser Technol. **135**, 106688 (2021).
17. R. Paschotta, J. Nilsson, A. C. Tropper, and D. C. Hanna, "Ytterbium-doped fiber amplifiers," IEEE J. quantum electronics **33**, 1049–1056 (1997).
18. M. E. Fermann and I. Hartl, "Ultrafast fiber laser technology," IEEE J. Sel. Top. Quantum Electron. **15**, 191–206 (2009).
19. O. Okhotnikov, L. Gomes, N. Xiang, T. Jouhti, and A. Grudinin, "Mode-locked ytterbium fiber laser tunable in the 980–1070-nm spectral range," Opt. letters **28**, 1522–1524 (2003).
20. C. Nielsen, B. Ortaç, T. Schreiber, J. Limpert, R. Hohmuth, W. Richter, and A. Tünnermann, "Self-starting self-similar all-polarization maintaining Yb-doped fiber laser," Opt. Express **13**, 9346–9351 (2005).
21. M. Baumgartl, F. Jansen, F. Stutzki, C. Jauregui, B. Ortaç, J. Limpert, and A. Tünnermann, "High average and peak power femtosecond large-pitch photonic-crystal-fiber laser," Opt. letters **36**, 244–246 (2011).
22. M. Baumgartl, J. Abreu-Afonso, A. Díez, M. Rothhardt, J. Limpert, and A. Tünnermann, "Environmentally stable picosecond Yb fiber laser with low repetition rate," Appl. Phys. B **111**, 39–43 (2013).
23. P. Deslandes, M. Perrin, J. Saby, D. Sangla, F. Salin, and E. Freysz, "Picosecond to femtosecond pulses from high power self mode–locked ytterbium rod-type fiber laser," Opt. express **21**, 10731–10738 (2013).
24. C. Cuadrado-Laborde, A. Carrascosa, A. Díez, J. Cruz, and M. Andrés, "All Polarization-maintaining Passively Mode-locked Ytterbium-doped Fiber Lasers, Behavior under Two Different Cavity Configurations," Fiber Integr. Opt. **39**, 240–252 (2020).
25. N. G. Usechak, G. P. Agrawal, and J. D. Zuegel, "Tunable, high-repetition-rate, harmonically mode-locked ytterbium fiber laser," Opt. letters **29**, 1360–1362 (2004).
26. H. Pask, R. J. Carman, D. C. Hanna, A. C. Tropper, C. J. Mackechnie, P. R. Barber, and J. M. Dawes, "Ytterbium-doped silica fiber lasers: versatile sources for the 1-1.2 μm region," IEEE J. Sel. Top. Quantum Electron. **1**, 2–13 (1995).
27. L. A. Gomes, L. Orsila, T. Jouhti, and O. G. Okhotnikov, "Picosecond SESAM-based ytterbium mode-locked fiber lasers," IEEE J. selected topics quantum electronics **10**, 129–136 (2004).
28. L. Kong, X. Xiao, and C. Yang, "Tunable all-normal-dispersion yb-doped mode-locked fiber lasers," Laser physics **20**, 834–837 (2010).
29. W. Liu, J. Fan, C. Xie, Y. Song, C. Gu, L. Chai, C. Wang, and M. Hu, "Programmable controlled mode-locked fiber laser using a digital micromirror device," Opt. Lett. **42**, 1923–1926 (2017).
30. C. Ma, A. Khanolkar, and A. Chong, "High-performance tunable, self-similar fiber laser," Opt. letters **44**, 1234–1236 (2019).
31. V. Matsas, T. Newson, D. Richardson, and D. N. Payne, "Selfstarting passively mode-locked fibre ring soliton laser exploiting nonlinear polarisation rotation," Electron. Lett. **28**, 1391–1393 (1992).
32. A. Chong, W. H. Renninger, and F. W. Wise, "Properties of normal-dispersion femtosecond fiber lasers," JOSA B **25**, 140–148 (2008). Number: 2 Publisher: Optical Society of America.
33. R. Xu, F. Xu, Y. Song, L. Duan, Y. Song, S. Tan, and Z. Liu, "Impact of spectral filtering on pulse breaking-up and noise-like pulse generation in all-normal dispersion fiber lasers," Opt. Express **28**, 21348–21358 (2020).
34. G. P. Agrawal, "Nonlinear fiber optics (fourth edition)," (Academic Press, 2006), Optics and Photonics, pp. 51–78, 4th ed.
35. C. H. Camp Jr, Y. J. Lee, J. M. Heddleston, C. M. Hartshorn, A. R. H. Walker, J. N. Rich, J. D. Lathia, and M. T. Cicerone, "High-speed coherent Raman fingerprint imaging of biological tissues," Nat. Photonics **8**, 627–634 (2014).
36. H. Rigneault and P. Berto, "Tutorial: Coherent Raman light matter interaction processes," APL Photonics **3**, 091101 (2018).